

**Journal of Geophysical Research: Atmospheres****RESEARCH ARTICLE**

10.1002/2015JD024503

**Key Points:**

- Interannual variability in cloud radiative effects is driven by midlevel and high clouds
- Wind-related feedbacks on natural aerosol emissions enhance this variability by 3 to 5%
- Variations in natural aerosol concentrations enhance interannual variability by 1 to 3%

**Supporting Information:**

- Supporting Information S1

**Correspondence to:**L. M. Russell,  
lmrussell@ucsd.edu**Citation:**

Yang, Y., et al. (2016), Impacts of ENSO events on cloud radiative effects in preindustrial conditions: Changes in cloud fraction and their dependence on interactive aerosol emissions and concentrations, *J. Geophys. Res. Atmos.*, 121, 6321–6335, doi:10.1002/2015JD024503.

Received 13 NOV 2015

Accepted 16 MAY 2016

Accepted article online 19 MAY 2016

Published online 2 JUN 2016

## Impacts of ENSO events on cloud radiative effects in preindustrial conditions: Changes in cloud fraction and their dependence on interactive aerosol emissions and concentrations

Yang Yang<sup>1,2</sup>, Lynn M. Russell<sup>1</sup>, Li Xu<sup>1</sup>, Sijia Lou<sup>1</sup>, Maryam A. Lamjiri<sup>1</sup>, Richard C. J. Somerville<sup>1</sup>, Arthur J. Miller<sup>1</sup>, Daniel R. Cayan<sup>1</sup>, Michael J. DeFlorio<sup>1</sup>, Steven J. Ghan<sup>3</sup>, Ying Liu<sup>3</sup>, Balwinder Singh<sup>3</sup>, Hailong Wang<sup>3</sup>, Jin-Ho Yoon<sup>4</sup>, and Philip J. Rasch<sup>3</sup>

<sup>1</sup>Scripps Institution of Oceanography, University of California, San Diego, La Jolla, California, USA, <sup>2</sup>Now at Atmospheric Science and Global Change Division, Pacific Northwest National Laboratory, Richland, Washington, USA, <sup>3</sup>Atmospheric Science and Global Change Division, Pacific Northwest National Laboratory, Richland, Washington, USA, <sup>4</sup>Gwangju Institute of Science and Technology, Gwangju, South Korea

**Abstract** We use three 150 year preindustrial simulations of the Community Earth System Model to quantify the impacts of El Niño–Southern Oscillation (ENSO) events on shortwave and longwave cloud radiative effects ( $\text{CRE}_{\text{SW}}$  and  $\text{CRE}_{\text{LW}}$ ). Compared to recent observations from the Clouds and the Earth's Radiant Energy System data set, the model simulation successfully reproduces larger variations of  $\text{CRE}_{\text{SW}}$  and  $\text{CRE}_{\text{LW}}$  over the tropics. The ENSO cycle is found to dominate interannual variations of cloud radiative effects. Simulated cooling (warming) effects from  $\text{CRE}_{\text{SW}}$  ( $\text{CRE}_{\text{LW}}$ ) are strongest over the tropical western and central Pacific Ocean during warm ENSO events, with the largest difference between 20 and 60  $\text{W m}^{-2}$ , with weaker effects of 10–40  $\text{W m}^{-2}$  over Indonesian regions and the subtropical Pacific Ocean. Sensitivity tests show that variations of cloud radiative effects are mainly driven by ENSO-related changes in cloud fraction. The variations in midlevel and high cloud fractions each account for approximately 20–50% of the interannual variations of  $\text{CRE}_{\text{SW}}$  over the tropics and almost all of the variations of  $\text{CRE}_{\text{LW}}$  between 60°S and 60°N. The variation of low cloud fraction contributes to most of the variations of  $\text{CRE}_{\text{SW}}$  over the midlatitude oceans. Variations in natural aerosol concentrations explained 10–30% of the variations of both  $\text{CRE}_{\text{SW}}$  and  $\text{CRE}_{\text{LW}}$  over the tropical Pacific, Indonesian regions, and the tropical Indian Ocean. Changes in natural aerosol emissions and concentrations enhance 3–5% and 1–3% of the variations of cloud radiative effects averaged over the tropics.

### 1. Introduction

Clouds strongly influence the Earth's radiation balance. They reflect incoming solar radiation back to space, which enhances the reflected solar flux by  $47.5 \pm 3 \text{ W m}^{-2}$  globally, and absorb outgoing infrared radiation, which reduces the outgoing longwave flux relative to clear sky by approximately  $26.4 \pm 4 \text{ W m}^{-2}$ . Overall, clouds exert a net cooling effect of about  $-21.1 \pm 5 \text{ W m}^{-2}$  at the top of atmosphere (TOA) [Stephens *et al.*, 2012], which is 6 times larger than that from doubling  $\text{CO}_2$  concentration [Ramanathan *et al.*, 1989; Loeb *et al.*, 2009]. Any changes in cloud properties such as cloud fraction, cloud top height, and microphysical features would perturb cloud radiative forcing and greatly modulate the radiative balance of the Earth system [Slingo, 1990; Wielicki *et al.*, 1998; Curry *et al.*, 2000; Stephens, 2005]. The Intergovernmental Panel on Climate Change reported that simulations of clouds and their radiative feedbacks are still one of the largest uncertainties in the fifth-generation climate models [Boucher *et al.*, 2013].

On interannual time scales, many regional changes in the global climate system are associated with the El Niño–Southern Oscillation (ENSO). ENSO is characterized by anomalous sea surface temperatures (SSTs) in the equatorial Pacific and has far-reaching impacts on global and regional temperature, precipitation, and circulation. Using cloud data from the Extended Edited Cloud Reports Archive (EECRA) from year 1954 to recent years, Park and Leovy [2004] and Eastman *et al.* [2011] both showed that interannual variations of cloud cover in the tropics have strong correlations to the ENSO index. For example, warmer central and eastern tropical Pacific SST (warm ENSO phase, i.e., El Niño) is associated with increased cloud cover in the tropical central Pacific Ocean and reduced cloud cover over the Indonesian and eastern Pacific regions, and vice versa for cool ENSO phase (La Niña) events.

ENSO's influence on cloud fraction typically varies with height. Zhu *et al.* [2007] showed that thick low cloud fraction decreased more than 20% in the tropical eastern Pacific during the 1997–1998 El Niño event, which was associated with an upward large-scale motion and a weak atmospheric stability. However, thin high cloud fraction was found to increase over the tropical Pacific and decrease over Indonesian regions during El Niño events compared to those during La Niña events [Norris, 2005; Marchand, 2013]. The mean vertical distribution of clouds is also sensitive to ENSO events. Zelinka and Hartmann [2011] and Lelli *et al.* [2014] reported that the vertical distribution of tropical clouds shifts upward during warm ENSO events.

Due to anomalous tropical atmospheric conditions during ENSO events, cloud radiative effects exhibit year-to-year differences. Moore and Vonder Haar [2001] examined the interannual variability of net cloud radiative effects from 1984 to 1990 using radiative flux data from the Earth Radiation Budget Experiment (ERBE). They found that during the El Niño season of 1986/1987, Pacific basin and global net cloud cooling effects were reduced by  $0.90 \text{ W m}^{-2}$  and  $1.29 \text{ W m}^{-2}$ , respectively, compared to those during the La Niña season of 1988/1989. Kato [2009] examined the interannual variation of the global radiation budget using the Clouds and the Earth's Radiant Energy System (CERES) data set from 2000 to 2004. He found that large anomalies in TOA shortwave and longwave fluxes over the tropical western and central Pacific were associated with changes in ENSO phase and that clouds are mostly responsible for the observed year-to-year variations. Loeb *et al.* [2007] also reported that most of the variability in CERES TOA flux is driven by variations in global cloud fraction, as observed using coincident CERES and the Moderate Resolution Imaging Spectrometer (MODIS) data between 2000 and 2005. The TOA radiation balance is sensitive to cloud heights, since low clouds exert cooling effects on the TOA, while high clouds exert warming effects. However, previous studies have not evaluated the contributions of clouds at different heights to interannual variations of cloud radiative effects.

Aerosols are another component of the atmosphere that substantially perturbs the Earth's radiative balance. Aerosol particles affect the climate system directly by scattering and absorbing solar radiation and indirectly by altering cloud microphysical properties [Twomey 1974; Albrecht, 1989; Lohmann and Feichter, 2005]. Climate variability, such as changes in ENSO phase, can influence the concentrations and distribution of aerosols and trace gases through changing their emissions, deposition, and transport [Chandra *et al.*, 1998, 2009; Prospero and Lamb, 2003; Ziemke and Chandra, 2003; Logan *et al.*, 2008; Mitchell *et al.*, 2010; Li *et al.*, 2011; Hsu *et al.*, 2012; Wu *et al.*, 2013; Yang *et al.*, 2014, 2015; Lou *et al.*, 2015; Xu *et al.*, 2015; DeFlorio *et al.*, 2016]. Using Sea-viewing Wide Field-of-view Sensor (SeaWiFS) measurements from 1997 to 2010, Hsu *et al.* [2012] found a high correlation between ENSO Index and monthly aerosol optical depth (AOD) anomalies over the Indonesian regions. With MODIS and Global Precipitation Climatology Project data from 2000 to 2010, Wu *et al.* [2013] reported that warm ENSO events are associated with aerosol increases over the Indonesian regions resulting from suppressed precipitation, which reduces the wet scavenging of aerosols and promotes dry conditions favorable for fire burning.

The influence of ENSO on aerosols is not confined to local tropical Pacific regions. Prospero and Lamb [2003] suggested that increased remote concentrations of Barbados summer dust might be related to warm ENSO events in the previous winter, which promote remote zonal teleconnection patterns in atmospheric circulation and precipitation over Africa and favor increased dust emission and subsequent westward transport. Mitchell *et al.* [2010] also found that Australian dust emission may be enhanced by El Niño-induced dry conditions. DeFlorio *et al.* [2016] suggested that westward transport of North African dust during summer is stronger during intense La Niña events, further emphasizing that the role ENSO can potentially play in remotely forcing year-to-year changes in the spatiotemporal distribution of aerosols.

Li *et al.* [2011] retrieved the column-average Ångström exponent from MODIS, the Multiangle Imaging Spectroradiometer and SeaWiFS for the period 2000–2011. The Ångström exponent is often used as a qualitative indicator of aerosol particle size. They showed that increases in Ångström exponent over the tropical western Pacific during El Niño events resulted from reductions of sea salt emissions and aerosol transport associated with surface wind anomalies. Van der Werf *et al.* [2006] and Logan *et al.* [2008] showed that a significant increase in biomass burning emissions occurred because of the enhanced fires in Indonesia during El Niño events.

These ENSO-related variations of natural aerosol emissions and concentrations also have potential impacts on the interannual variations of cloud radiative effects. However, few previous studies have considered the

role of variations in natural aerosols when investigating interannual variations of cloud radiative effects. Studies that addressed interannual variations of cloud radiative effects have been constrained by relatively short (10 year) satellite data, which only contain a few cycles of interannual variability. Consequently, the conclusions drawn from using these data sets are subject to sampling error. Extensive model simulations with realistic ENSO physics can be used to estimate the interannual variations of cloud radiative effects. In addition, the roles of ENSO-related variations in cloud fraction at different heights and variations in natural aerosols due to interactive emissions and concentrations can be explored and can potentially provide a better understanding of climate variability and contribute to improved predictions of tropical climate.

We present here a systematic investigation of the interannual variations of cloud radiative effects based on a set of three 150 year simulations in preindustrial conditions using the Community Earth System Model (CESM). We quantify (1) the observed and simulated interannual variations of cloud radiative effects; (2) their relationship with ENSO events; and (3) the contributions of natural aerosol variability and cloud fraction at various vertical levels to interannual variations in cloud radiative effects.

The CESM model and numerical experiments are described in section 2. Section 3 provides an overview of the simulated interannual variations of cloud radiative effects and comparisons to observations. Section 4 investigates ENSO-related interannual variations of cloud radiative effects by comparing simulations with and without interactive emissions and concentrations of natural aerosols. Section 5 shows the contributions of cloud fractions and natural aerosols to the interannual variations of cloud radiative effects. Section 6 summarizes these results.

## 2. Model Description and Experimental Design

Simulations in preindustrial conditions were performed using CESM. The atmospheric model resolution is  $1.9^{\circ}$  latitude by  $2.5^{\circ}$  longitude with 30 vertical layers ranging from the surface to 3.6 hPa (see supporting information). The CESM treats the properties and processes of major aerosol species (sea salt, mineral dust, sulfate, black carbon, primary organic matter, and secondary organic aerosol) in the modal aerosol module (MAM3) [Liu et al., 2012]. A more detailed description of the model aerosol representation can be found in Liu et al. [2012]. Stratiform cloud microphysics predicts number and mass mixing ratios of droplets and ice crystals and diagnoses number and mass mixing ratios of rain and snow as described by Liu et al. [2007], Morrison and Gettelman [2008], and Gettelman et al. [2010]. The treatment of deep and shallow convective cloud parameterizations is described in Zhang and McFarlane [1995] and Park and Bretherton [2009], respectively. Cloud macrophysical processes are represented according to Park et al. [2014].

To quantify the simulated relationships between ENSO and cloud radiative effects and to identify the contributions of natural aerosol variability and cloud fraction at various vertical levels to interannual variations in cloud radiative effects, the following 150 year simulations are performed:

1. IRUN. The standard simulation of preindustrial conditions using interactive ("I") emissions, deposition, and transport. Emissions and concentrations of natural aerosols are allowed to interact with meteorological fields.
2. ERUN. The sensitivity simulation of preindustrial conditions using prescribed emissions ("E") of natural aerosols. The emissions of sea salt aerosol used in the simulation are interpolated in time between the 12 monthly mean values derived from the 150 year IRUN simulation, and they are not changed by the actual yearly values of wind and temperature. Hence, this simulation contains no interannual variability of sea salt emissions. The model setup conditions are otherwise the same as those in IRUN.
3. CRUN. The sensitivity simulation of preindustrial conditions using prescribed aerosol concentrations. The concentrations of all aerosol components are interpolated in time between the 12 monthly mean values derived from the 150 year IRUN simulation. Hence, this simulation contains no interannual variability of aerosol concentration for all aerosol species. The model setup conditions are otherwise the same as those in IRUN.

The IRUN simulation is performed to evaluate the model ability to simulate interannual variations of cloud radiative effects when compared with observations; these simulations also allow investigation of the relationship between cloud radiative effects and ENSO events. By comparing results between the IRUN and ERUN simulations, the contributions of natural aerosol emission variability on the variations in cloud radiative

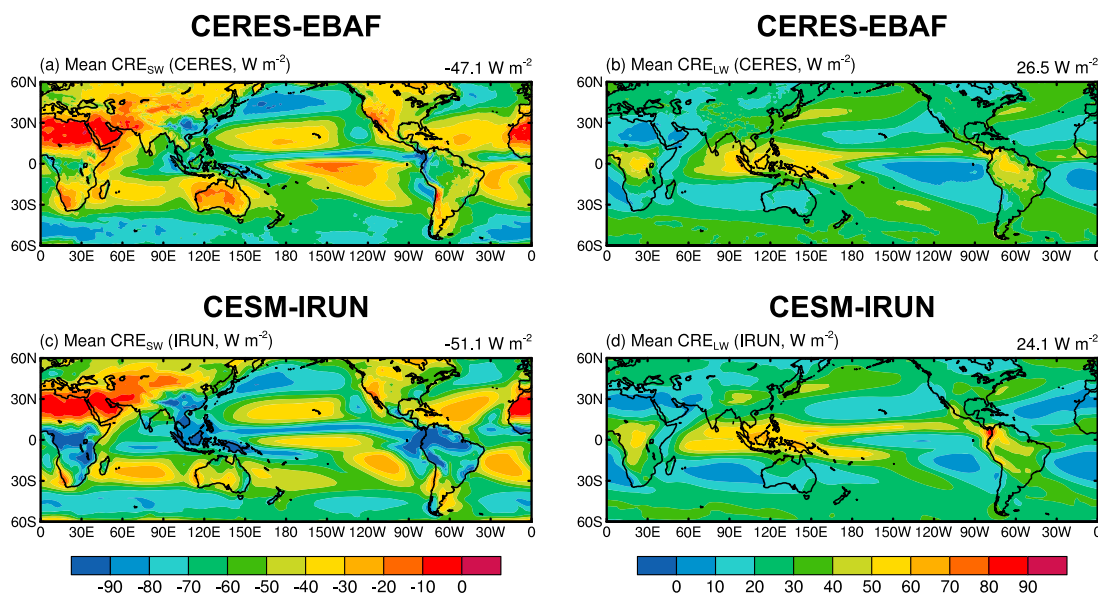


**Figure 1.** Observed mean of (a) shortwave and (b) longwave cloud radiative effects ( $\text{CRE}_{\text{SW}}$  and  $\text{CRE}_{\text{LW}}$ ) from Clouds and the Earth's Radiant Energy System Energy Balanced and Filled data set (CERES-EBAF) for years 2001–2014, and simulated climatological mean (c) shortwave and (d) longwave cloud radiative effects from IRUN simulation of CESM model. Global area-weighted mean values of cloud radiative effects are presented at the top right corner of each panel.

effects are identified. The roles of natural aerosol concentration variability on the variations in cloud radiative effects are then examined by comparing results between IRUN and CRUN. It is worth noting that, in the ERUN simulation, the variations in natural aerosol emission variability are removed by fixing sea salt emissions, which might cause some artificial biases because variations in other natural aerosol and their precursor emissions may still lead to variations in cloud radiative effects.

In this work, we focus on the interannual variations of cloud radiative effects in preindustrial conditions (for the year 1850 emissions), because much of the uncertainty in aerosol indirect forcing arises from uncertainties in natural aerosols [Carslaw *et al.*, 2013]. The fire emissions have no interannual variations in any of the simulations. Only regions between 60°S and 60°N are analyzed in this study because the cloud radiative effects over the polar regions are highly affected by sea ice and snow [Kato, 2009; Dong *et al.*, 2010]. The cloud radiative effect (CRE) is defined as the difference of net downward radiative flux between all sky and clear sky at the TOA, with positive (negative) cloud radiative effect indicating that the cloud warms (cools) the underlying atmosphere and surface [Ramanathan *et al.*, 1989].

### 3. Simulated Interannual Variations of Cloud Radiative Effects

The observed and simulated annual shortwave and longwave cloud radiative effects ( $\text{CRE}_{\text{SW}}$  and  $\text{CRE}_{\text{LW}}$ ) are shown in Figure 1 and Figure S1 (see supporting information). CESM successfully reproduces the observed maximum value of annual  $\text{CRE}_{\text{SW}}$  and  $\text{CRE}_{\text{LW}}$  over the tropics, as well as large  $\text{CRE}_{\text{SW}}$  over the midlatitude oceans and the subtropical eastern Pacific Ocean. The simulated global climatological mean  $\text{CRE}_{\text{SW}}$  and  $\text{CRE}_{\text{LW}}$  from IRUN is  $-51.1$  and  $24.1 \text{ W m}^{-2}$ , respectively. These values are in agreement with satellite observations ( $-47.1$  and  $26.5 \text{ W m}^{-2}$  from CERES Energy Balanced and Filled (CERES-EBAF) [Loeb *et al.*, 2009] and  $-54.2$  and  $30.4 \text{ W m}^{-2}$  from ERBE [Harrison *et al.*, 1990] for  $\text{CRE}_{\text{SW}}$  and  $\text{CRE}_{\text{LW}}$ , respectively) and multimodel mean values ( $-51.4$  and  $26.0 \text{ W m}^{-2}$  from the Coupled Model Intercomparison Project Phase 5 [Dolinar *et al.*, 2015]). Note that model simulations are based on aerosol emissions in the year 1850, whereas observations refer to the present-day aerosol emissions. This introduces some differences between the model simulations and observations that may be related to the aerosol differences.

Standard deviations of observed  $\text{CRE}_{\text{SW}}$  and  $\text{CRE}_{\text{LW}}$  from CERES-EBAF satellite observations for years 2001–2014 as well as those from model simulations are plotted in Figure 2. In this work, the standard deviation is used to represent the magnitude of variation, which is calculated with monthly anomalies of  $\text{CRE}_{\text{SW}}$  and  $\text{CRE}_{\text{LW}}$  for each

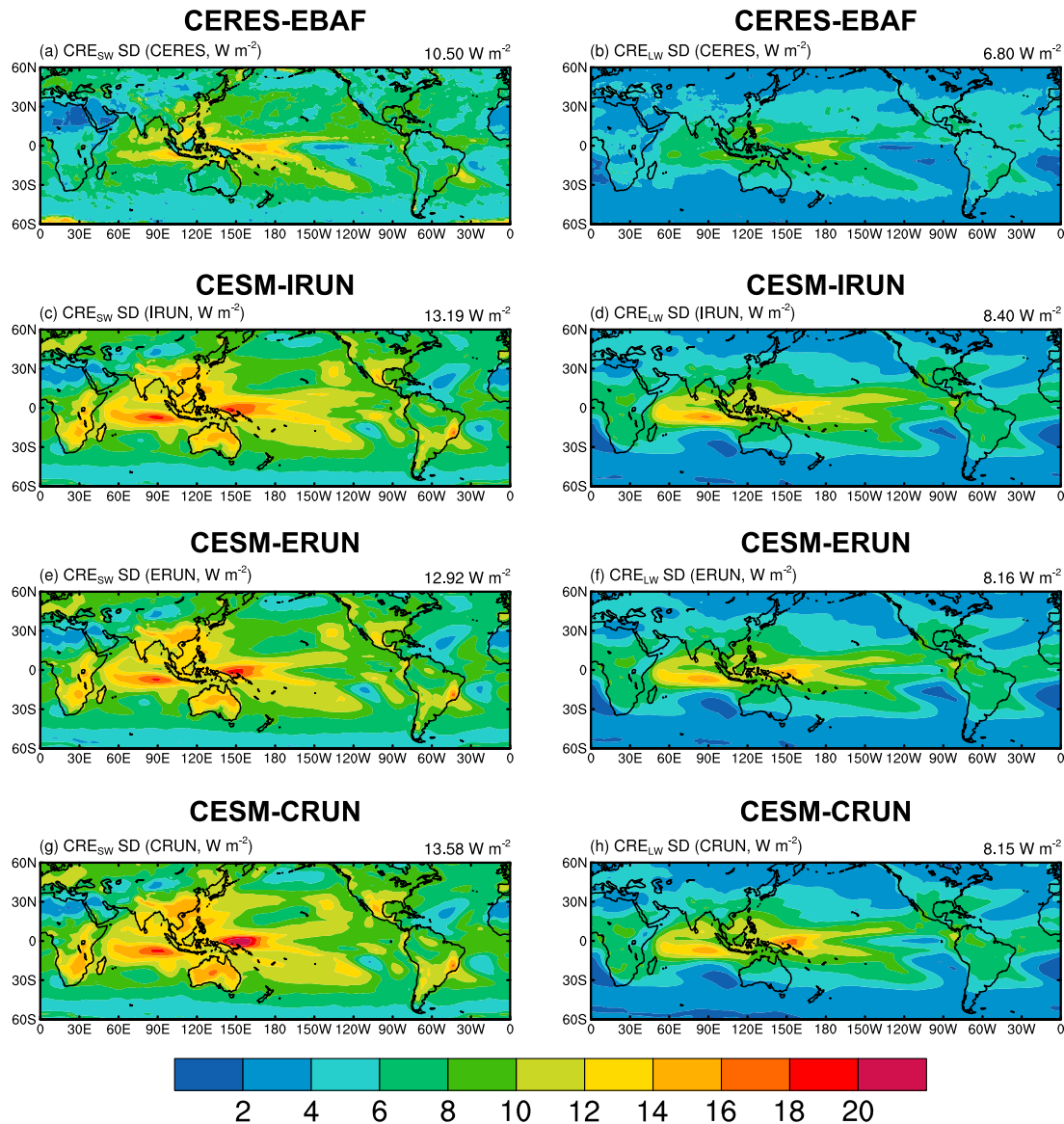


**Figure 2.** Standard deviation of observed (a)  $\text{CRE}_{\text{SW}}$  and (b)  $\text{CRE}_{\text{LW}}$  from Clouds and the Earth's Radiant Energy System Energy Balanced and Filled data set (CERES-EBAF) for years 2001–2014, and standard deviation of simulated (c, e, g)  $\text{CRE}_{\text{SW}}$  and (d, f, h)  $\text{CRE}_{\text{LW}}$  cloud radiative effects from IRUN, ERUN, and CRUN using CESM model. Global ( $60^{\circ}\text{S}$ – $60^{\circ}\text{N}$ ) area-weighted mean of standard deviations computed from monthly anomalies for each grid box is given at the top right corner of each panel.

grid over the 150 year model record. The standard deviation of simulated  $\text{CRE}_{\text{SW}}$  is largest over the tropical western and central Pacific Ocean, the eastern Pacific Ocean, the tropical Indian Ocean, and parts of Europe, East Asia, Africa, Australia, North and South America (Figure 2c), which is consistent with observations (Figure 2a), with maximum variations exceeding  $18 \text{ W m}^{-2}$ . The largest variations of  $\text{CRE}_{\text{SW}}$  are located over  $150^{\circ}\text{E}$  and  $165^{\circ}\text{E}$  in the equatorial Pacific Ocean in IRUN and observations, respectively. The global ( $60^{\circ}\text{S}$ – $60^{\circ}\text{N}$ , hereafter) area-weighted mean value of the simulated  $\text{CRE}_{\text{SW}}$  standard deviation computed from monthly anomalies over each grid is  $13.2 \text{ W m}^{-2}$  for preindustrial conditions in IRUN, which is larger than  $10.5 \text{ W m}^{-2}$  from present-day observation. For simulated  $\text{CRE}_{\text{LW}}$ , large standard deviation values are located mainly within the tropics, with maximum values over the tropical western and central Pacific and the tropical Indian Ocean (Figure 2d), which also have a positive bias over the tropics compared to observations (Figure 2a). The global area-weighted mean value of the simulated  $\text{CRE}_{\text{LW}}$  standard deviation in IRUN is  $8.4 \text{ W m}^{-2}$ , larger than observed value of  $6.8 \text{ W m}^{-2}$ . Overall, the model realistically captures the spatial distribution of observed interannual variations of  $\text{CRE}_{\text{SW}}$  and  $\text{CRE}_{\text{LW}}$ , with global spatial pattern correlation coefficients of 0.76 and 0.84, respectively. However, the model

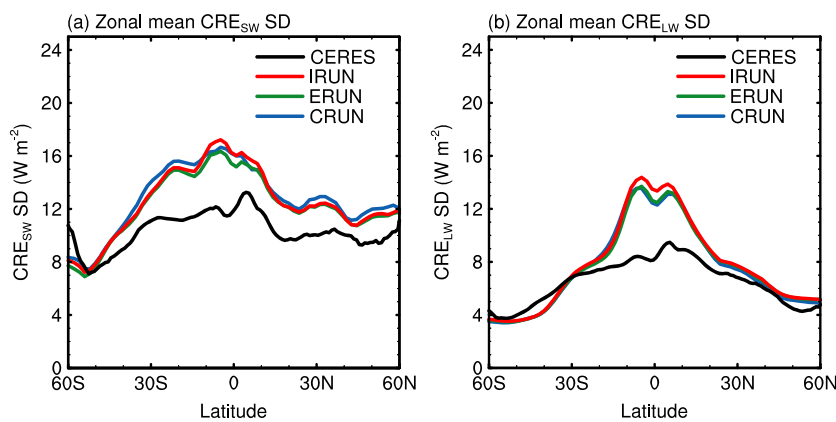


**Figure 3.** Observed and simulated zonal mean of standard deviation of (a)  $\text{CRE}_{\text{SW}}$  and (b)  $\text{CRE}_{\text{LW}}$ . Black line represents values from CERES-EBAF observations. Red, green, and blue lines represent values from the IRUN, ERUN, and CRUN of CESM model simulations.

overestimates the observed variations both in  $\text{CRE}_{\text{SW}}$  and  $\text{CRE}_{\text{LW}}$  by 23–36% globally. For fixed natural aerosol emissions, the global area-weighted mean of standard deviation is reduced by 2–3% for ERUN (Figures 2e and 2f) relative to those in IRUN. With fixed aerosol concentrations, the model produces more variations of cloud radiative effects over the western equatorial Pacific Ocean, with global area-weighted mean values of simulated standard deviations for  $\text{CRE}_{\text{SW}}$  and  $\text{CRE}_{\text{LW}}$  of  $13.6$  and  $8.2 \text{ W m}^{-2}$  (Figures 2g and 2h).

In order to examine the interannual variations of cloud radiative effects from both observations and simulations for different latitudinal bands, the zonal mean of the standard deviation of simulated and observed  $\text{CRE}_{\text{SW}}$  and  $\text{CRE}_{\text{LW}}$  are presented in Figure 3. The model reproduces the observed spatial variability of  $\text{CRE}_{\text{SW}}$  and  $\text{CRE}_{\text{LW}}$ , with the largest standard deviation over the tropics and decreasing values as the latitude increases (see supporting information). Notably, the standard deviations of  $\text{CRE}_{\text{SW}}$  and  $\text{CRE}_{\text{LW}}$  over the tropics from IRUN are larger than those from ERUN and CRUN simulations, suggesting that variations of natural aerosols play an important role in influencing interannual variations of  $\text{CRE}_{\text{SW}}$  and  $\text{CRE}_{\text{LW}}$ . Averaged over the tropics ( $20^{\circ}\text{S}$ – $20^{\circ}\text{N}$ ), the mean standard deviation of  $\text{CRE}_{\text{SW}}$  ( $\text{CRE}_{\text{LW}}$ ) are  $15.2$  ( $11.8$ ),  $14.8$  ( $11.3$ ), and  $15.1$  ( $11.5$ )  $\text{W m}^{-2}$  in IRUN, ERUN, and CRUN, respectively. With interactive sea salt emissions in IRUN, the model

simulated 3–5% higher variations over the tropics compared to the ERUN simulation, and interactive natural aerosol concentrations in IRUN increased variations of cloud radiative effects by 1–3% relative to the CRUN simulation.

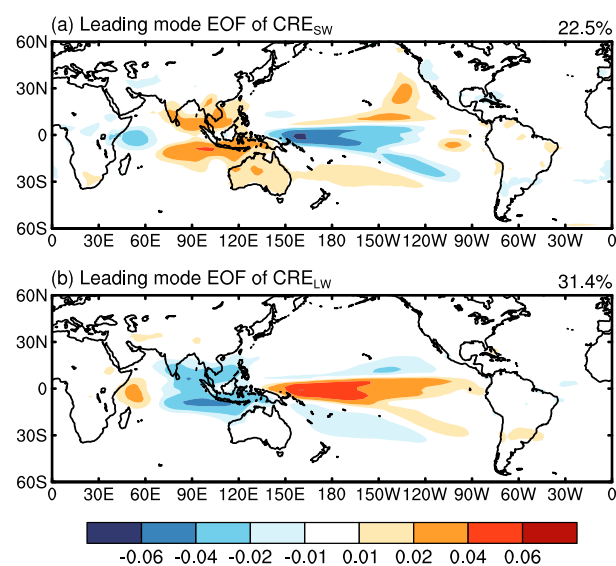


**Figure 4.** The leading EOF mode of simulated yearly (a)  $\text{CRE}_{\text{SW}}$  and (b)  $\text{CRE}_{\text{LW}}$  in the IRUN simulation. The variance explained by the leading mode EOF is given at the top right corner of each panel.

#### 4. ENSO-Related Interannual Variations of Cloud Radiative Effects

To explore the interannual variations of cloud radiative effects, we calculated empirical orthogonal functions (EOFs) of yearly anomalies of the simulated  $\text{CRE}_{\text{SW}}$  and  $\text{CRE}_{\text{LW}}$ . The leading EOF of yearly  $\text{CRE}_{\text{SW}}$  and  $\text{CRE}_{\text{LW}}$  anomalies for the 150 year IRUN simulation are shown in Figure 4. The leading EOFs explain 22.5% and 31.4% of the interannual variations of simulated  $\text{CRE}_{\text{SW}}$  and  $\text{CRE}_{\text{LW}}$ , respectively. The variability is generally largest over regions in the  $30^{\circ}\text{S}$  to

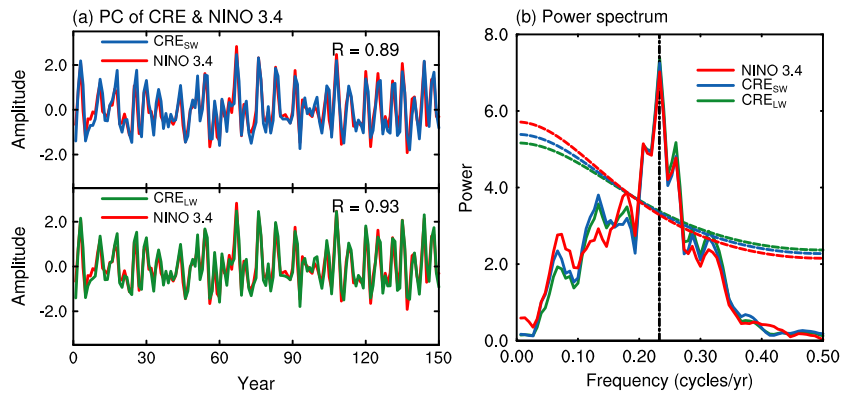


**Figure 5.** (a) The time series of principal components (PCs) of leading mode EOF (corresponding to EOF in Figure 3) of simulated CRE<sub>SW</sub> (blue line) and CRE<sub>LW</sub> (green line) and Niño 3.4 Index (red line). (b) The power spectrum of PCs of EOF of simulated CRE<sub>SW</sub> and CRE<sub>LW</sub> and power spectrum of Niño 3.4 Index. Correlation coefficient between Niño 3.4 Index and PCs of EOF of CRE<sub>SW</sub>/CRE<sub>LW</sub> is shown in the top right corner in each panel of Figure 5a. The corresponding dashed lines in Figure 5b indicate the 95% significance levels. CRE<sub>SW</sub>, CRE<sub>LW</sub>, and Niño 3.4 Index are computed from IRUN simulation.

30°N latitudinal band for both CRE<sub>SW</sub> and CRE<sub>LW</sub>. In this region, most of the observed climate variability is associated with ENSO phenomena (see supporting information).

The leading principal components (PCs) that correspond to the leading EOF mode of CRE<sub>SW</sub> and CRE<sub>LW</sub> (shown in Figure 4) and the time series of the Niño 3.4 Index calculated from the simulated SST are shown in Figure 5a. The Niño 3.4 Index is the averaged SST anomaly over Niño 3.4 region (5°S–5°N, 170–120°W), which is one of several ENSO indicators and is used to characterize the intensity of an ENSO event. The leading PCs are strongly correlated with the Niño 3.4 Index, with correlation coefficients of 0.89 (0.93), which are statistically significant at the 95th percentile. These strong correlations demonstrate that the ENSO cycle has strong impacts on interannual variations of cloud radiative effects.

To further investigate the relationship between the ENSO cycle and interannual variations of cloud radiative effects, we show the power spectrum of the modeled Niño 3.4 Index as well as the leading PCs of yearly CRE<sub>SW</sub> and CRE<sub>LW</sub> anomalies in Figure 5b. The Niño 3.4 Index shows a significant peak at a frequency of

0.23 cycles per year, suggesting that the simulated ENSO occurs on a time scale of about 4.3 years. It is in the range of the observed ENSO period, which ranges from 2 to 7 years with an average value of approximately 4 years [MacMynowski and Tziperman, 2008]. The PCs of the leading EOF of CRE<sub>SW</sub> and CRE<sub>LW</sub> display the same peak of 0.23 cycles per year with the Niño 3.4 Index. This similarity in the cycle frequency indicates that ENSO has a strong effect on the interannual variations of cloud radiative effects between 60°S and 60°N. Spatial patterns of the correlation coefficients between monthly anomalies of CRE<sub>SW</sub> (CRE<sub>LW</sub>) and the Niño 3.4 index are almost the same as the patterns of the EOF, with statistically significant values mainly between 30°S and 30°N, as shown in Figure 6. Spatial patterns of the correlation coefficients between the PCs of the leading EOF mode of CRE<sub>SW</sub> (CRE<sub>LW</sub>) and SST monthly anomaly also show significant

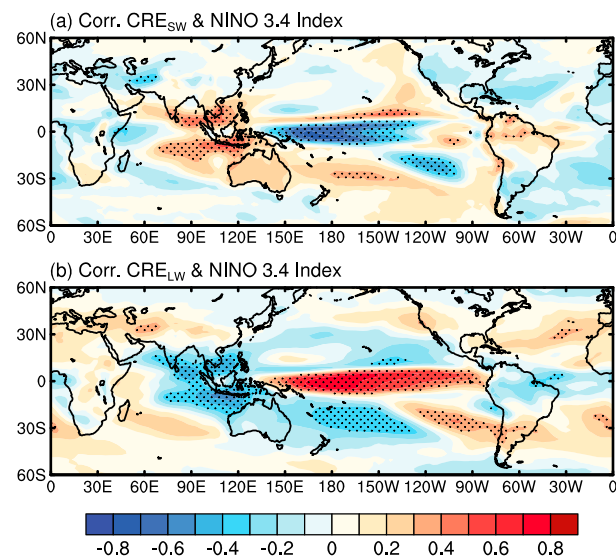


**Figure 6.** Spatial distribution of the correlation coefficients between month anomalies of (a) CRE<sub>SW</sub> and (b) CRE<sub>LW</sub> and monthly Niño 3.4 Index. Cloud radiative effects and Niño 3.4 Index are computed from IRUN simulation. The dotted areas indicate statistical significance with 95% confidence from a two-tailed Student's *t* test.

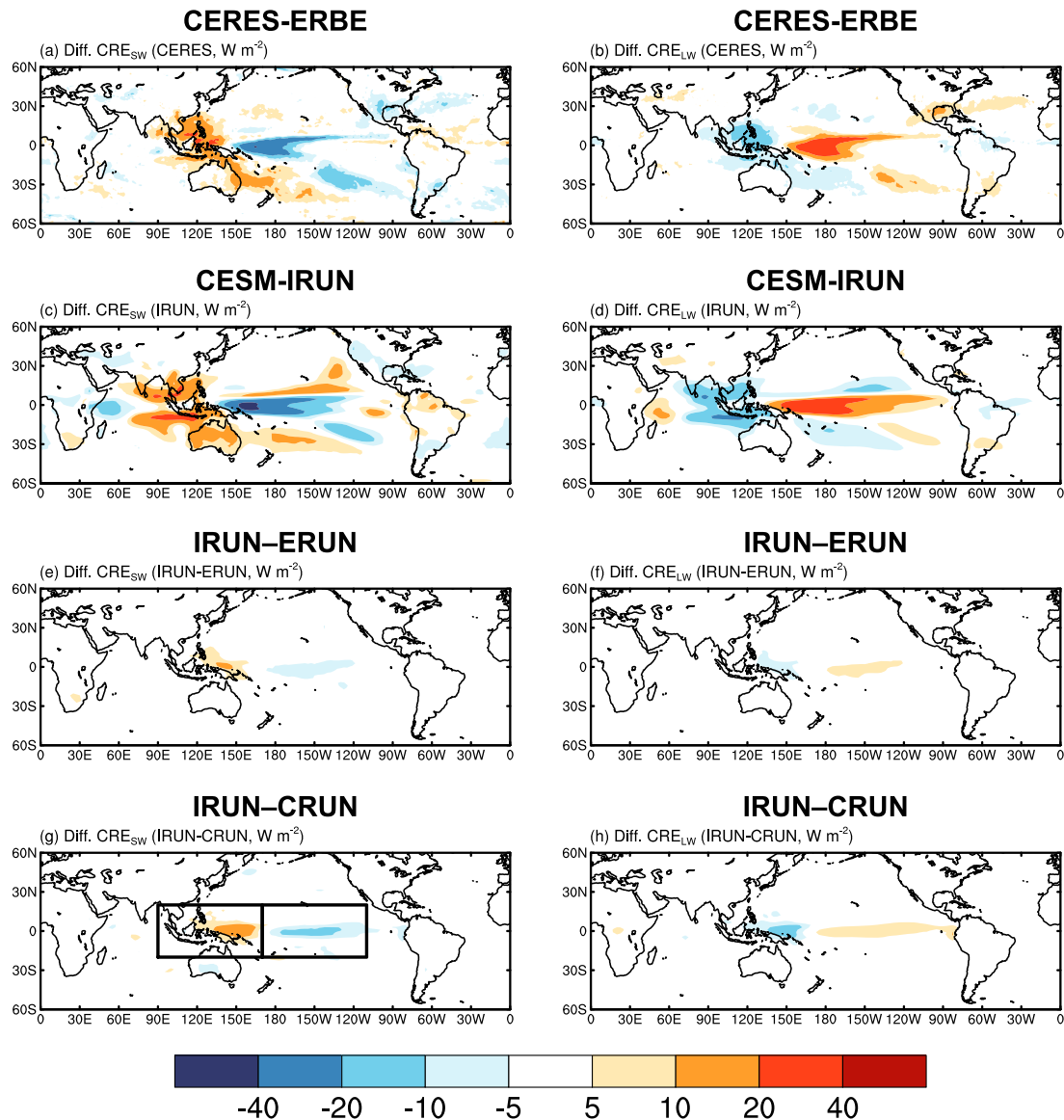


**Figure 7.** Composite differences in (a, b) observed and (c, d) simulated (left column)  $\text{CRE}_{\text{SW}}$  and (right column)  $\text{CRE}_{\text{LW}}$  from CERES-EBAF satellite data and IRUN simulation, as well as the changes of these differences due to changes in (e, f) natural aerosol emissions (IRUN-ERUN) and (g, h) concentrations (IRUN-CRUN) on  $\text{CRE}_{\text{SW}}$  and  $\text{CRE}_{\text{LW}}$  between El Niño and La Niña events. Observed monthly Niño 3.4 Index are calculated using surface air temperature from NCEP/NCAR (National Centers for Environmental Prediction/National Center for Atmospheric Research) reanalysis data. The location boxes ( $90^{\circ}\text{E}$ – $170^{\circ}\text{E}$ ,  $20^{\circ}\text{S}$ – $20^{\circ}\text{N}$  and  $170^{\circ}\text{E}$ – $110^{\circ}\text{W}$ ,  $20^{\circ}\text{S}$ – $20^{\circ}\text{N}$ ) selected to capture the features of changes in  $\text{CRE}_{\text{SW}}$  and  $\text{CRE}_{\text{LW}}$  in the Indonesian regions and the tropical western Pacific, as well as the tropical eastern and central Pacific between El Niño and La Niña events are also shown in Figure 7g.

ENSO signal (Figure S2). These further imply a close relationship between the ENSO cycle and the interannual variations of cloud radiative effects.

To quantify the impacts of ENSO events on cloud radiative effects, we show the composite differences in observed and simulated  $\text{CRE}_{\text{SW}}$  and  $\text{CRE}_{\text{LW}}$  between El Niño events and La Niña events (see supporting information) in Figure 7, in addition to the changes in  $\text{CRE}_{\text{SW}}$  and  $\text{CRE}_{\text{LW}}$  caused by variations of natural aerosol emissions and concentrations. Relative to those during La Niña events, simulated cooling (warming) effects from  $\text{CRE}_{\text{SW}}$  ( $\text{CRE}_{\text{LW}}$ ) during El Niño events from IRUN are stronger over the tropical western and central Pacific Ocean, with the largest difference between 20 and  $60 \text{ W m}^{-2}$  (Figures 7c and 7d). Simulated  $\text{CRE}_{\text{SW}}$  ( $\text{CRE}_{\text{LW}}$ ) during El Niño events have weaker cooling (warming) effects than those during La Niña events by  $10$ – $40 \text{ W m}^{-2}$  over the Indonesian regions and the subtropical Pacific Ocean. The pattern of the composite differences in cloud radiative effects agrees with the leading EOF mode pattern (Figure 4).

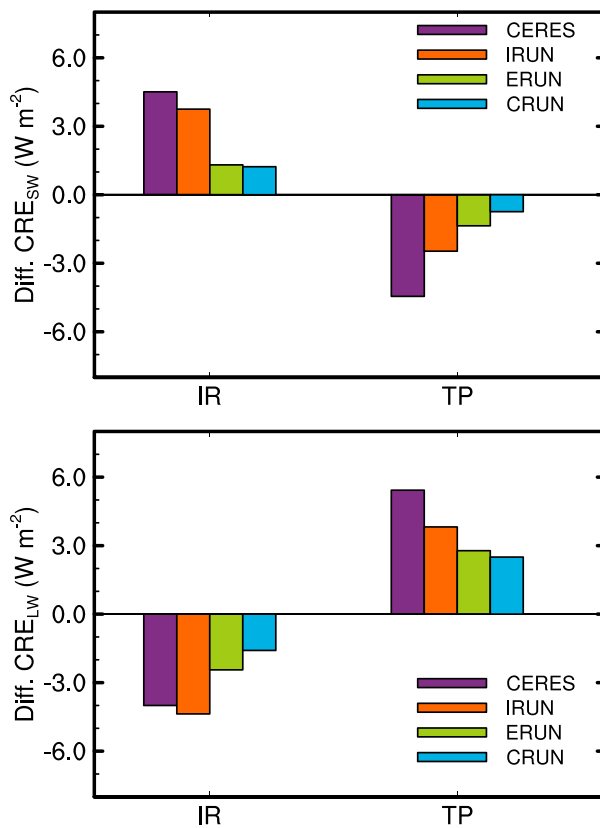


**Figure 8.** Composite differences in simulated (top)  $\text{CRE}_{\text{SW}}$  and (bottom)  $\text{CRE}_{\text{LW}}$  over the Indonesian regions and the tropical western Pacific (IR,  $90^{\circ}\text{E}$ – $170^{\circ}\text{E}$ ,  $20^{\circ}\text{S}$ – $20^{\circ}\text{N}$ ), and the tropical eastern and central Pacific (TP,  $170^{\circ}\text{E}$ – $110^{\circ}\text{W}$ ,  $20^{\circ}\text{S}$ – $20^{\circ}\text{N}$ ) between El Niño and La Niña events from CERES-EBAF data set, and the IRUN, ERUN, and CRUN simulations.

ing) effect of  $\text{CRE}_{\text{SW}}$  ( $\text{CRE}_{\text{LW}}$ ) by  $10$ – $20 \text{ W m}^{-2}$ , whereas the  $\text{CRE}_{\text{SW}}$  ( $\text{CRE}_{\text{LW}}$ ) effect is enhanced over the tropical central Pacific Ocean. Between  $150$  and  $160^{\circ}\text{E}$  in the equatorial Pacific Ocean, the simulated cooling (warming) effect of  $\text{CRE}_{\text{SW}}$  ( $\text{CRE}_{\text{LW}}$ ) is stronger during El Niño events (Figures 7c and 7d), whereas the natural aerosol variability leads to a warming (cooling) effect over this region (Figures 7g and 7h), resulting in the smaller  $\text{CRE}_{\text{SW}}$  ( $\text{CRE}_{\text{LW}}$ ) variability in IRUN (Figures 2c and 2d) than those in CRUN simulation (Figures 2g and 2h). Over the tropical central and eastern Pacific Ocean, the natural aerosol variability enhances the cooling (warming) effect of  $\text{CRE}_{\text{SW}}$  ( $\text{CRE}_{\text{LW}}$ ), resulting in the larger zonal  $\text{CRE}_{\text{SW}}$  ( $\text{CRE}_{\text{LW}}$ ) variability in IRUN than those in CRUN simulation over the tropics (Figures 3a and 3b). It is noticeable that influence of natural aerosol variability on  $\text{CRE}_{\text{SW}}$  and  $\text{CRE}_{\text{LW}}$  is mainly over the tropical Indian Ocean and tropical western Pacific Ocean on interannual time scales, and its role is less important over the midlatitude and the tropical eastern Pacific, which is due to the interactions between sea salt and ENSO strength and is examined in Y. Yang et al. (Variations in sea salt emissions enhance ENSO strength, submitted to *Journal of Climate*, 2016).

To examine the roles of variations in natural aerosol emissions and concentrations on cloud radiative effects, observed and simulated composite differences of  $\text{CRE}_{\text{SW}}$  and  $\text{CRE}_{\text{LW}}$  averaged over the Indonesian regions and the tropical western Pacific Ocean ( $90$ – $170^{\circ}\text{E}$ ,  $20^{\circ}\text{S}$ – $20^{\circ}\text{N}$ ), and the tropical eastern and central Pacific Ocean ( $170^{\circ}\text{E}$ – $110^{\circ}\text{W}$ ,  $20^{\circ}\text{S}$ – $20^{\circ}\text{N}$ ) are presented in Figure 8. Over the Indonesian regions and the tropical western Pacific Ocean, the composite difference of simulated  $\text{CRE}_{\text{SW}}$  ( $\text{CRE}_{\text{LW}}$ ) between El Niño and La Niña events in IRUN is  $3.8$  ( $-4.4$ )  $\text{W m}^{-2}$ . With fixed natural aerosol emissions and concentrations, the magnitude of this difference decreases to  $1.3$  ( $-2.4$ )  $\text{W m}^{-2}$  and  $1.2$  ( $-1.6$ )  $\text{W m}^{-2}$  in ERUN and CRUN, respectively. Over the eastern and central Pacific Ocean, the composite difference of simulated  $\text{CRE}_{\text{SW}}$  ( $\text{CRE}_{\text{LW}}$ ) is  $-2.5$  ( $3.8$ )  $\text{W m}^{-2}$  in IRUN. The magnitude of this difference also decreases in ERUN and CRUN. These results indicate

Compared to the composite differences in observed  $\text{CRE}_{\text{SW}}$  and  $\text{CRE}_{\text{LW}}$  between El Niño and La Niña events from the CERES-EBAF satellite data (Figures 7a and 7b), the model realistically simulates the observed spatial distribution of these differences (Figures 7b and 7c), although some values over the equatorial Pacific, two bands off the equator, and the tropical eastern Indian Ocean are overpredicted, due to the biases in simulating cloud fraction over these regions. The model captures the largest observed changes over Indonesian regions and the tropical western and central Pacific Ocean, which are due to the large annual mean cloud fraction and ENSO-induced cloud fraction variability over these regions. Variations in natural aerosol emissions between El Niño and La Niña events slightly enhance the cooling (warming) effect of  $\text{CRE}_{\text{SW}}$  ( $\text{CRE}_{\text{LW}}$ ) over the tropical Pacific Ocean and weaken this effect over the Indonesian regions, with magnitudes in the range of  $5$ – $10 \text{ W m}^{-2}$  (IRUN–ERUN, Figures 7e and 7f). The changes of  $\text{CRE}_{\text{SW}}$  and  $\text{CRE}_{\text{LW}}$  resulting from variations in natural aerosol concentrations (IRUN–CRUN, Figures 7g and 7h) are larger than those due to variations in emissions. Over eastern Indonesian regions and the tropical western Pacific Ocean, changes in natural aerosol concentrations reduced the cooling (warm-

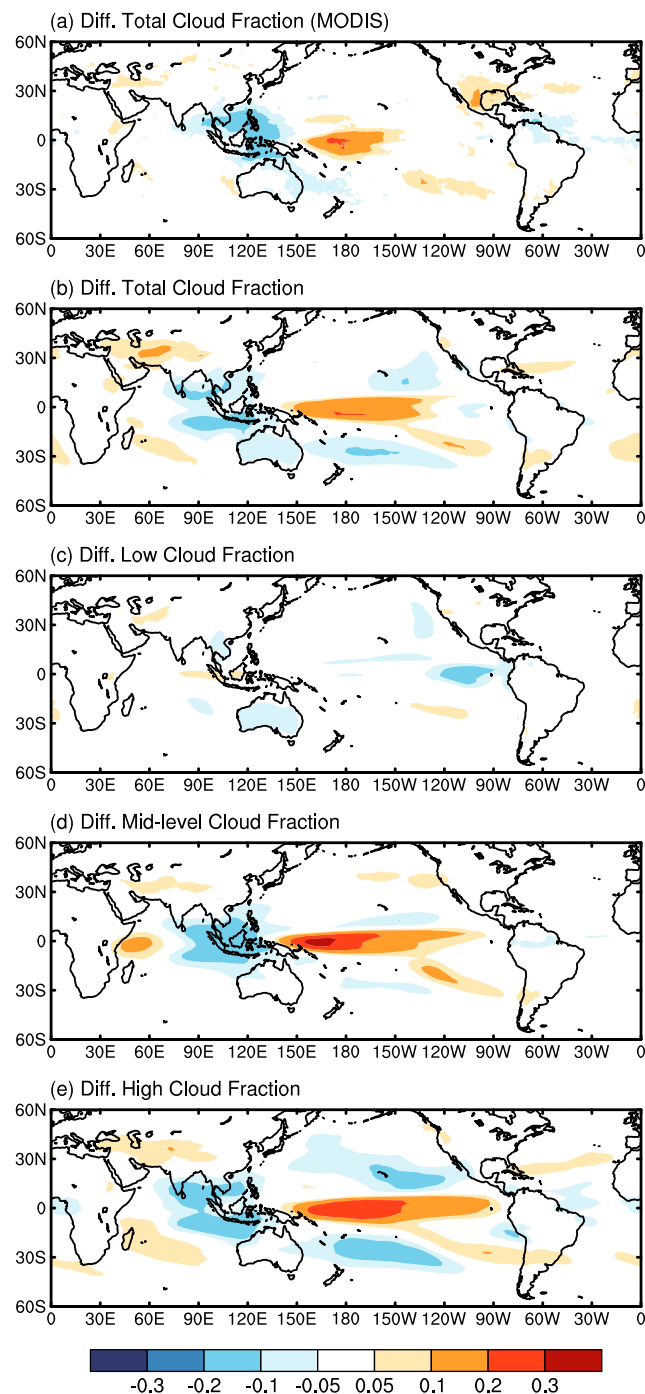


**Figure 9.** Composite differences in (a) observed and (b) simulated total cloud fraction and simulated (c) low, (d) midlevel, and (e) high cloud fraction between El Niño and La Niña events. Low, midlevel, and high clouds are clouds in pressure ranges of 1200–700, 700–400, and 400–50 hPa, respectively. Observed cloud fractions are from the Moderate Resolution Imaging Spectrometer (MODIS) for years 2001 to 2014. Simulated cloud fraction is from the 150 year IRUN simulation.

radiative effects between 30°S and 30°N. Differences in total, midlevel, and high cloud fractions between El Niño and La Niña events from the ERUN and CRUN simulations are slightly larger than those from the IRUN simulation over the tropical western Pacific and smaller over the tropical eastern Pacific (Figure S3). This result

that variations in natural aerosol emissions and concentrations are associated with larger differences in cloud radiative effects over the tropics.

## 5. Contributions of ENSO-Related Cloud Fractions and Natural Aerosols

Variations in cloud radiative effects are largely affected by variations in cloud fraction [Loeb *et al.*, 2007; Kato, 2009], which correlate strongly with ENSO patterns in the tropics [Park and Leovy, 2004; Eastman *et al.*, 2011; Zelinka and Hartmann, 2011]. The composite differences in observed total cloud fraction between El Niño and La Niña events from MODIS for years 2001–2014, as well as simulated values from the IRUN simulation are shown in Figures 9a and 9b. The model realistically reproduces the pattern of larger cloud fraction over the tropical western and central Pacific Ocean and lower cloud fraction over the Indonesian regions during El Niño events relative to those during La Niña events, although it overpredicts values off the equator and over the tropical eastern Indian Ocean (see supporting information).

Composite differences between El Niño and La Niña events from the IRUN simulation in low, midlevel, and high cloud fractions, respectively, are presented in Figures 9c–9e. Relative to those in La Niña events, the low cloud fraction during El Niño events decreases over the tropical eastern and central Pacific Ocean, whereas midlevel and high cloud fractions increase over this region, consistent with observations [Norris, 2005; Zhu *et al.*, 2007; Marchand, 2013]. Differences in midlevel and high cloud fractions between El Niño and La Niña events are largest between 30°S and 30°N and are similar to differences in total cloud fraction. This suggests that changes in midlevel and high cloud fractions, which dominate the variation of total cloud fraction, have large influences on the interannual variations of cloud

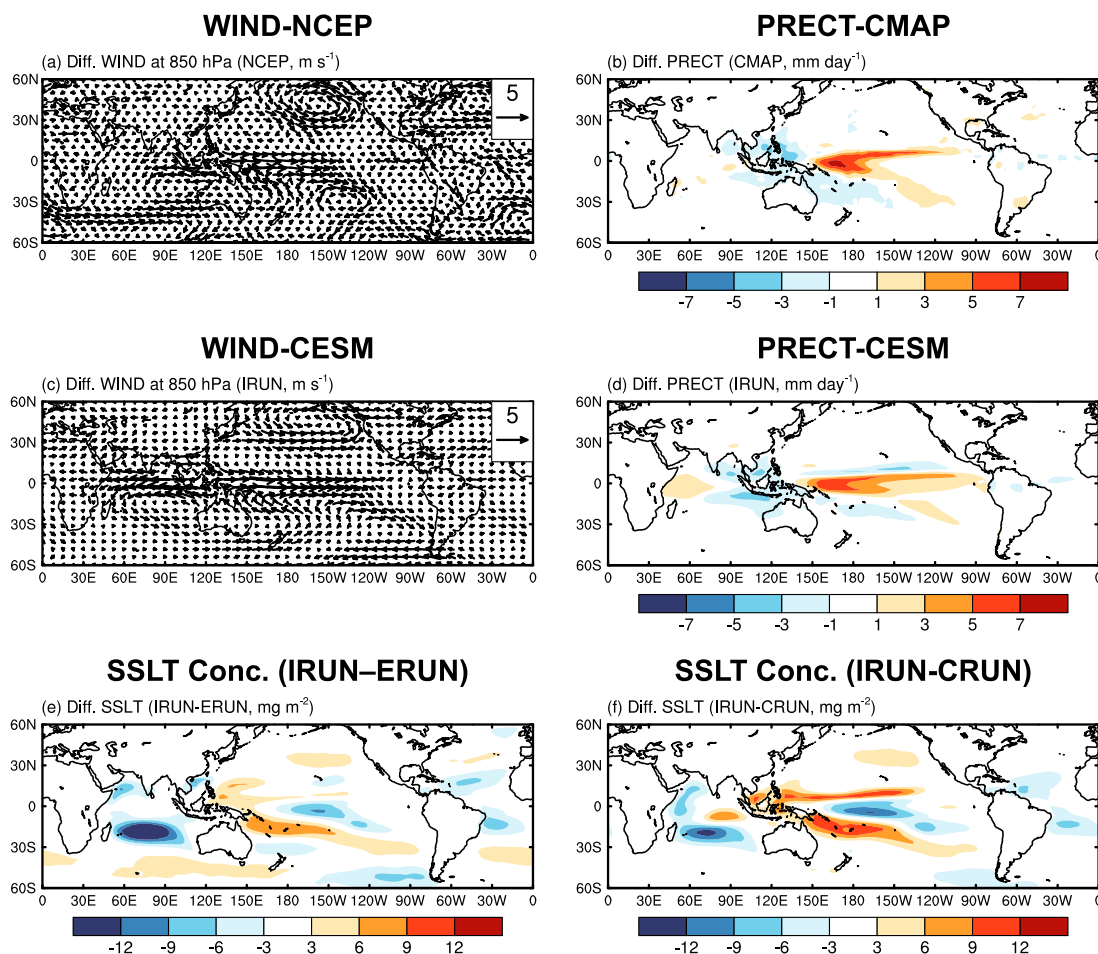


**Figure 10.** Composite differences in wind field at 850 hPa from (a) NCEP/NCAR reanalysis data set and (c) IRUN simulation, as well as differences in (b) observed and (d) simulated precipitation rate from CMAP data and IRUN simulation between El Niño and La Niña events. The changes in composite differences in sea salt (SSLT) concentrations between El Niño and La Niña events (e) between IRUN and ERUN and (f) between IRUN and CRUN simulations.

indicates that although changes in cloud fraction are driven by changes in meteorology, changes in natural aerosol emissions and concentrations may also influence cloud fraction and can further perturb cloud radiative effects.

Previous findings have identified changes in aerosols as the main drivers of global dimming and brightening [Streets *et al.*, 2009; Ruckstuhl *et al.*, 2008; Cermak *et al.*, 2010]. After evaluating the role of changes in SST on variations of marine cloud, Eastman *et al.* [2011] suggested that changes in aerosol concentrations in the atmosphere could also be a factor influencing cloud fraction. Composite differences of observed and simulated wind fields at 850 hPa between El Niño and La Niña events from the NCEP/NCAR (National Centers for Environmental Prediction/National Center for Atmospheric Research) reanalysis data for years 2001–2014 [Kalnay *et al.*, 1996] and the IRUN simulation are plotted in Figures 10a and 10c. During El Niño events, easterly winds are reduced over the tropical Pacific. The changes in sea salt concentrations caused by changes in sea salt emissions show a similar pattern, which decrease over the tropical central Pacific Ocean and increase over the subtropical Pacific Ocean (Figure 10e), similar to the findings of Xu *et al.* [2015].

In addition to emissions, changes in natural aerosol concentrations are primarily driven by wet scavenging and transport processes, which are manifested in the precipitation and wind fields, respectively. The changes in sea salt concentrations between El Niño and La Niña events are found to be mainly influenced by wet deposition (Figures S4 and S5, see supporting information). The composite differences in observed and simulated precipitation rate between El Niño and La Niña events from the CMAP (Climate Prediction Center's Merged Analysis of Precipitation) data set for years 2001–2014 [Xie and Arkin, 1997] and the IRUN

simulation are shown in Figures 10b and 10d. The model adeptly reproduces the observed pattern of increasing precipitation over the tropical Pacific Ocean, with the largest difference of  $6\text{--}8 \text{ mm d}^{-1}$  over the tropical western Pacific Ocean and decreasing precipitation over the Indonesian regions. The difference of ERUN and CRUN compared to IRUN is that interannual variability of emissions of sea salt in ERUN and concentrations of all aerosol species in CRUN are excluded in these two sensitivity simulations, respectively. Besides emissions, changes in precipitation also lead to lower sea salt concentrations over the tropical Pacific Ocean and higher concentrations over the Indonesian regions between El Niño and La Niña events (Figure 10f).

The spatial distribution and relative sign of these changes in the sea salt concentrations resulting from interactive natural aerosol emissions (Figure 10e) and concentrations (Figure 10f) are similar to those of changes in cloud radiative effects (Figures 7e and 7g, and Figures 7f and 7h). This reaffirms that natural aerosol variability can influence interannual variations in cloud radiative effects, probably through changing the incoming solar radiation or other ocean dynamic processes. This needs to be examined in future studies.

To estimate the contribution of ENSO-related variations in cloud fractions and natural aerosols to the interannual variations of cloud radiative effects, we used a multivariate regression for both  $\text{CRE}_{\text{SW}}$  and  $\text{CRE}_{\text{LW}}$  in the IRUN simulation, similar to the approach of Xu *et al.* [2015] (see supporting information). The low, middle-level, and high cloud fractions, and column burden concentration of sea salt are chosen as predictors. The total variance explained by the regressions ( $R^2$ ) are presented in Figure S6. The regressions account for 80% and 82% of  $\text{CRE}_{\text{SW}}$  and  $\text{CRE}_{\text{LW}}$  variability, respectively, averaged over regions between  $60^\circ\text{S}$  and  $60^\circ\text{N}$ , as well as 90% and 86% averaged between  $30^\circ\text{S}$  and  $30^\circ\text{N}$ .

In order to evaluate the contributions of predictors in linear models, we applied the LMG (Lindeman, Merenda, and Gold) method [Lindeman *et al.*, 1980; Grömping, 2006]. This method provides a decomposition of the model-explained variance into nonnegative contributions. The estimated fraction of annual variance in  $\text{CRE}_{\text{SW}}$  and  $\text{CRE}_{\text{LW}}$  explained by the low, middlelevel, and high cloud fractions, as well as sea salt concentration using the LMG method, are shown in Figure 11. Over the tropics, the variations in midlevel and high cloud fractions each account for about 20–50% of the interannual variations of  $\text{CRE}_{\text{SW}}$  (Figures 11c and 11e). This results from large variations in midlevel and high cloud fractions during ENSO events. In the midlatitude oceans, the interannual variations of  $\text{CRE}_{\text{SW}}$  are primarily driven by low cloud fraction variability (Figure 11a) due to the important role of marine stratocumulus over these regions. Note that, although low cloud fraction drives the  $\text{CRE}_{\text{SW}}$  variability over the midlatitude oceans, the  $\text{CRE}_{\text{SW}}$  variability is smaller than that over the tropics (Figures 2a and 2c) due to the lower cloud fraction variability over the midlatitude oceans (Figures 9a and 9b). For  $\text{CRE}_{\text{LW}}$ , almost all variations between  $60^\circ\text{S}$  and  $60^\circ\text{N}$  are contributed by the midlevel and high cloud fraction variability (Figures 11d and 11f), whereas the low cloud fraction variability exerts little effect (Figure 11b) since  $\text{CRE}_{\text{LW}}$  are primarily driven by midlevel and high clouds. The variation in sea salt concentration explains 10–30% of the interannual variations of both  $\text{CRE}_{\text{SW}}$  and  $\text{CRE}_{\text{LW}}$  over the tropical Pacific Ocean, the Indonesian regions, and the tropical Indian Ocean (Figures 11g and 11h).

In this study, the simulated interannual variations in cloud radiative effects are larger than those from the present-day observations, especially over the tropics (Figure 3). This is due to the model overestimation of ENSO events on the one hand. On the other hand, it is worth noting that observations are at the present-day conditions for only 14 years from 2001 to 2014, which is a constraint on studying interannual atmospheric variations in a robust way. Furthermore, present-day observations may not fully represent the variability in cloud radiative effects at preindustrial conditions.

## 6. Conclusions

One hundred fifty year simulations in preindustrial conditions with the CESM model showed interannual variations of cloud radiative effects with features that are characteristic of the El Niño–Southern Oscillation (ENSO) events. The interannual variations of shortwave and longwave cloud radiative effects at the top of atmosphere ( $\text{CRE}_{\text{SW}}$  and  $\text{CRE}_{\text{LW}}$ ) are quantified using standard deviation values. The model produces large variations in  $\text{CRE}_{\text{SW}}$  over the tropical western and central Pacific, the eastern Pacific, the tropical Indian Ocean, as well as parts of Europe, East Asia, Africa, Australia, North and South America, similar to what is observed in CERES observations, with maximum variations exceeding  $18 \text{ W m}^{-2}$ . The large variations of  $\text{CRE}_{\text{LW}}$  are located mainly within the tropics. The global area-weighted mean standard deviations of  $\text{CRE}_{\text{SW}}$

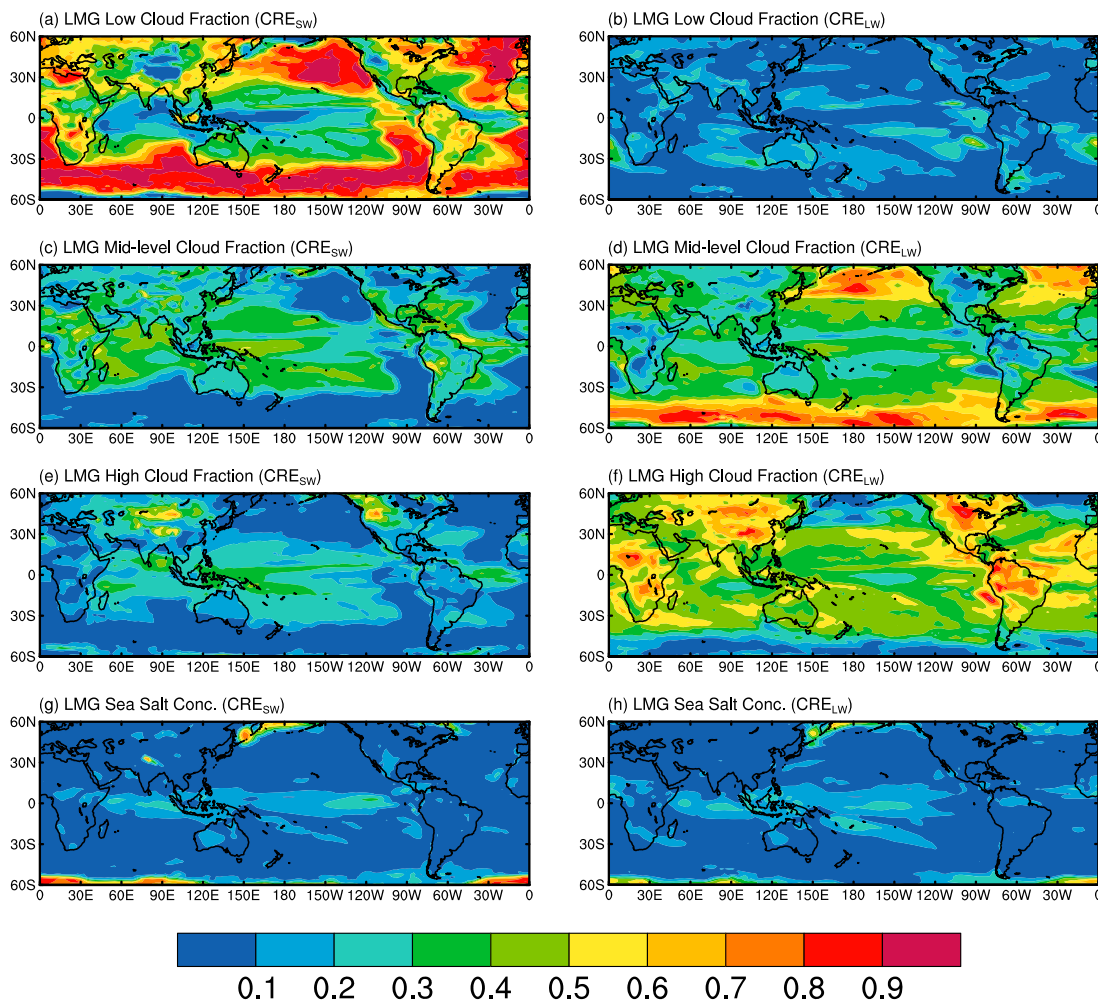


**Figure 11.** The LMG method for estimated fraction of annual variance in (left column)  $\text{CRE}_{\text{SW}}$  and (right column)  $\text{CRE}_{\text{LW}}$  explained by (a, b) low, (c, d) midlevel, and (e, f) high cloud fraction, and (g, h) sea salt concentrations from IRUN simulation.

and  $\text{CRE}_{\text{LW}}$  are  $13.2$  and  $8.4 \text{ W m}^{-2}$ , respectively. Both of these values are larger than the observed values of  $10.5$  and  $6.8 \text{ W m}^{-2}$  in present-day conditions.

Using EOF analysis, the leading PCs of simulated  $\text{CRE}_{\text{SW}}$  ( $\text{CRE}_{\text{LW}}$ ) are strongly correlated with the ENSO index. Correlation coefficients between the Niño 3.4 Index and the leading PCs of  $\text{CRE}_{\text{SW}}$  ( $\text{CRE}_{\text{LW}}$ ) are  $0.89$  ( $0.93$ ). Using spectral analysis, the power spectrum of the leading PCs of  $\text{CRE}_{\text{SW}}$  ( $\text{CRE}_{\text{LW}}$ ) showed the same peak with the Niño 3.4 Index at the frequency of  $0.23$  cycles per year, about  $4.3$  years per cycle. These results demonstrate that the ENSO is the only detectable cycle in the interannual variations of cloud radiative effects in the preindustrial atmosphere simulated by CESM. Relative to those during La Niña events, simulated cooling (warming) effects from  $\text{CRE}_{\text{SW}}$  ( $\text{CRE}_{\text{LW}}$ ) during El Niño events are stronger over the tropical western and central Pacific Ocean, with the largest difference between  $20$  and  $60 \text{ W m}^{-2}$ . In contrast, the cooling (warming) effects are weaker by  $10$ – $40 \text{ W m}^{-2}$  over the Indonesian regions and the subtropical Pacific Ocean.

The changes in cloud fraction are found to be mainly responsible for the variations of cloud radiative effects between El Niño and La Niña events. In a positive ENSO event (El Niño), the cloud fraction increases in the tropical western and central Pacific Ocean and decreases over the Indonesian regions, the tropical eastern Indian Ocean, the eastern Pacific Ocean, the southwest coast of North America, and the southern Pacific Ocean. Relative to those in La Niña events, the low cloud fraction during El Niño events decreases over the tropical eastern and central Pacific Ocean, whereas midlevel and high cloud fraction increases over this region, consistent with observations.

Changes in natural aerosol emissions and concentrations are found to partly contribute to the variations in cloud radiative effects. Variations in natural aerosol emissions between El Niño and La Niña events slightly enhance the cooling (warming) effect of  $\text{CRE}_{\text{SW}}$  ( $\text{CRE}_{\text{LW}}$ ) over the tropical Pacific Ocean and weaken this effect over the Indonesian regions, with magnitudes in the range of  $5\text{--}10 \text{ W m}^{-2}$ . Over eastern Indonesian regions and the tropical western Pacific Ocean, the cooling (warming) effect of  $\text{CRE}_{\text{SW}}$  ( $\text{CRE}_{\text{LW}}$ ) are reduced by  $10\text{--}20 \text{ W m}^{-2}$ , whereas the  $\text{CRE}_{\text{SW}}$  ( $\text{CRE}_{\text{LW}}$ ) effect is enhanced over the tropical central Pacific Ocean, mainly resulting from variations in natural aerosols concentrations. Considering the variations of cloud radiative effects caused by changes in cloud fraction, the variations in natural aerosol emissions and concentrations enhance 3–5% and 1–3% of variations in cloud radiative effects over the tropics, respectively.

The LMG method for the linear model used here suggests that the variability in midlevel and high cloud fractions each account for about 20–50% of the interannual variations of  $\text{CRE}_{\text{SW}}$  over the tropics and almost all of the interannual variations of  $\text{CRE}_{\text{LW}}$  between  $60^{\circ}\text{S}$  and  $60^{\circ}\text{N}$ . In the midlatitude oceans, the interannual variations of  $\text{CRE}_{\text{SW}}$  are primarily driven by low cloud fraction variability. The variations in sea salt concentrations explain 10–30% of the interannual variations of both  $\text{CRE}_{\text{SW}}$  and  $\text{CRE}_{\text{LW}}$  over the tropical Pacific Ocean, the Indonesian regions, and the tropical Indian Ocean.

This work shows the effects of natural aerosol emissions and concentrations on interannual variations of cloud radiative effects with and without interactive emissions and concentrations. However, there are still some uncertainties associated with the sensitivity simulations. Although cloud radiative effects have similar annual means for all simulations (Figure S1), the mean AOD and mean meteorological fields may have some differences. We present in Figure S7 the simulated climatological mean of AOD, SST, precipitation rate, and surface wind stress in IRUN, ERUN, and CRUN. While the AOD, precipitation rate, and surface stress are similar for all three configurations, surface temperature is 1 K lower in CRUN relative to IRUN. Although this sensitivity is noteworthy, it does not change our main conclusions about the role of aerosol variability in variability of other components of the climate system.

The combination of simulations with fully interactive aerosol, climatological mean emissions, and climatological mean concentrations could also be used to investigate the role of feedbacks of other aerosol sources with climate variability, such as dust, dimethyl sulfide, and carbonaceous aerosol from wild fires.

## Acknowledgments

This research was supported by NSF AGS1048995 and by DOE DE-SC0006679 as part of the U.S. Department of Energy, Office of Science, Biological and Environmental Research, Decadal and Regional Climate Prediction using Earth System Models (EaSM) program. The Pacific Northwest National Laboratory is operated for the DOE by Battelle Memorial Institute under contract DE-AC05-76RLO 1830. CMAP precipitation data and NCEP reanalysis data are provided by the NOAA/OAR/ESRL PSD, Boulder, Colorado, USA, from their Web site at <http://www.esrl.noaa.gov/psd/>. The National Energy Research Scientific Computing Center (NERSC) provided computational resources. The data and codes for these results are posted at [http://portal.nersc.gov/project/m1374/CRE\\_EaSM](http://portal.nersc.gov/project/m1374/CRE_EaSM).

## References

- Albrecht, B. A. (1989), Aerosols, cloud microphysics, and fractional cloudiness, *Science*, 245, 1227–1230, doi:10.1126/science.245.4923.1227.
- Boucher, O., et al. (2013), Clouds and aerosols, in *Climate Change 2013: The Physical Science Basis. Contribution of Working Group I to the Fifth Assessment Report of the Intergovernmental Panel on Climate Change*, edited by T. F. Stocker et al., Cambridge Univ. Press, Cambridge, U.K., and New York.
- Carslaw, K. S., et al. (2013), Large contribution of natural aerosols to uncertainty in indirect forcing, *Nature*, 503, 67–71, doi:10.1038/nature12674.
- Cermak, J., M. Wild, R. Knutti, M. I. Mishchenko, and A. K. Heidinger (2010), Consistency of global satellite-derived aerosol and cloud data sets with recent brightening observations, *Geophys. Res. Lett.*, 37, L21704, doi:10.1029/2010GL044632.
- Chandra, S., J. R. Ziemke, J. R. Min, and W. G. Read (1998), Effects of 1997–1998 El Niño on tropospheric ozone and water vapor, *Geophys. Res. Lett.*, 25, 3867–3870, doi:10.1029/98GL02695.
- Chandra, S., J. R. Ziemke, B. N. Duncan, T. L. Diehl, N. J. Livesey, and L. Froidevaux (2009), Effects of the 2006 El Niño on tropospheric ozone and carbon monoxide: Implications for dynamics and biomass burning, *Atmos. Chem. Phys.*, 9, 4239–4249, doi:10.5194/acp-9-4239-2009.
- Curry, J. A., et al. (2000), FIRE Arctic clouds experiment, *Bull. Am. Meteorol. Soc.*, 81, 5–29, doi:10.1175/1520-0477(2000)081<0005:FACE>2.3.CO;2.
- DeFlorio, M. J., I. D. Goodwin, D. R. Cayan, A. J. Miller, S. J. Ghan, D. W. Pierce, L. M. Russell, and B. Singh (2016), Interannual modulation of subtropical Atlantic boreal summer dust variability by ENSO, *Clim. Dyn.*, 46, 585–599, doi:10.1007/s00382-015-2600-7.
- Dolinar, E., X. Dong, B. Xi, J. Jiang, and H. Su (2015), Evaluation of CMIP5 simulated clouds and TOA radiation budgets using NASA satellite observations, *Clim. Dyn.*, 44, 2229–2247, doi:10.1007/s00382-014-2158-9.
- Dong, X., B. Xi, K. Crosby, C. N. Long, R. S. Stone, and M. D. Shupe (2010), A 10 year climatology of Arctic cloud fraction and radiative forcing at Barrow, Alaska, *J. Geophys. Res.*, 115, D17212, doi:10.1029/2009JD013489.
- Eastman, R., S. G. Warren, and C. J. Hahn (2011), Variations in cloud cover and cloud types over the ocean from surface observations. 1954–2008, *J. Clim.*, 24, 5914–5934, doi:10.1175/2011JCLI3972.1.
- Gettelman, A., X. Liu, S. J. Ghan, H. Morrison, S. Park, A. J. Conley, S. A. Klein, J. Boyle, D. L. Mitchell, and J.-F. L. Li (2010), Global simulations of ice nucleation and ice supersaturation with an improved cloud scheme in the Community Atmosphere Model, *J. Geophys. Res.*, 115, D18216, doi:10.1029/2009JD013797.
- Grömping, U. (2006), Relative importance for linear regression in R: The package relaimpo, *J. Stat.*, 17(1).
- Harrison, E., P. Minnis, B. Barkstrom, V. Ramanathan, R. Cess, and G. Gibson (1990), Seasonal variation of cloud radiative forcing derived from the Earth Radiation Budget Experiment, *J. Geophys. Res.*, 95, 18,687–18,703, doi:10.1029/JD095iD11p18687.
- Hsu, N. C., R. Gautam, A. M. Sayer, C. Bettenhausen, C. Li, M. J. Jeong, S.-C. Tsay, and B. N. Holben (2012), Global and regional trends of aerosol optical depth over land and ocean using SeaWiFS measurements from 1997 to 2010, *Atmos. Chem. Phys.*, 12, 8037–8053, doi:10.5194/acp-12-8037-2012.
- Kalnay, E., et al. (1996), The NCEP/NCAR 40-year reanalysis project, *Bull. Am. Meteorol. Soc.*, 77, 437–470, doi:10.1175/1520-0477(1996)077<0437:TNYRP>2.0.CO;2.

- Kato, S. (2009), Interannual variability of global radiation budget, *J. Clim.*, 22, 4893–4907, doi:10.1175/2009JCLI2795.1.
- Lelli, L., A. A. Kokhanovsky, V. V. Rozanov, M. Vountas, and J. P. Burrows (2014), Linear trends in cloud top height from passive observations in the oxygen A-band, *Atmos. Chem. Phys.*, 14, 5679–5692, doi:10.5194/acp-14-5679-2014.
- Li, J., B. E. Carlson, and A. A. Lacis (2011), El Niño–Southern Oscillation correlated aerosol Ångström exponent anomaly over the tropical Pacific discovered in satellite measurements, *J. Geophys. Res.*, 116, D20204, doi:10.1029/2011JD015733.
- Lindeman, R. H., P. F. Merenda, and R. Z. Gold (1980), *Introduction to Bivariate and Multivariate Analysis*, Scott, Foresman, Glenview, Ill.
- Liu, X., J. E. Penner, S. J. Ghan, and M. Wang (2007), Inclusion of ice microphysics in the NCAR community atmospheric model version 3 (CAM3), *J. Clim.*, 20, 4526–4547, doi:10.1175/JCLI4264.1.
- Liu, X., et al. (2012), Toward a minimal representation of aerosols in climate models: Description and evaluation in the Community Atmosphere Model CAM5, *Geosci. Model Dev.*, 5, 709–739, doi:10.5194/gmd-5-709-2012.
- Loeb, N. G., B. A. Wielicki, W. Su, K. Loukachine, W. Sun, T. Wong, K. J. Priestley, G. Matthews, W. F. Miller, and R. Davies (2007), Multi-instrument comparison of top of the atmosphere reflected solar radiation, *J. Clim.*, 20, 575–591, doi:10.1175/JCLI4018.1.
- Loeb, N. G., B. A. Wielicki, D. R. Doelling, G. L. Smith, D. F. Keyes, S. Kato, N. Manalo-Smith, and T. Wong (2009), Toward optimal closure of the Earth's top-of-atmosphere radiation budget, *J. Clim.*, 22, 748–766, doi:10.1175/2008JCLI2637.1.
- Logan, J. A., I. Megretskaya, R. Nassar, L. T. Murray, L. Zhang, K. W. Bowman, H. M. Worden, and M. Luo (2008), Effects of the 2006 El Niño on tropospheric composition as revealed by data from the Tropospheric Emission Spectrometer (TES), *Geophys. Res. Lett.*, 35, L03816, doi:10.1029/2007GL031698.
- Lohmann, U., and J. Feichter (2005), Global indirect aerosol effects: A review, *Atmos. Chem. Phys.*, 5, 715–737, doi:10.5194/acp-5-715-2005.
- Lou, S., H. Liao, Y. Yang, and Q. Mu (2015), Simulation of the interannual variations of tropospheric ozone over China: Roles of variations in meteorological parameters and anthropogenic emissions, *Atmos. Environ.*, doi:10.1016/j.atmosenv.2015.08.081, in press.
- MacMynowski, D. G., and E. Tziperman (2008), Factors affecting ENSO's period, *J. Atmos. Sci.*, 65, 1570–1586, doi:10.1175/2007JAS2520.1.
- Marchand, R. (2013), Trends in ISCCP, MISR, and MODIS cloud-top-height and optical-depth histograms, *J. Geophys. Res. Atmos.*, 118, 1941–1949, doi:10.1002/jgrd.50207.
- Mitchell, R. M., S. K. Campbell, and Y. Qin (2010), Recent increase in aerosol loading over the Australian arid zone, *Atmos. Chem. Phys.*, 10, 1689–1699, doi:10.5194/acp-10-1689-2010.
- Moore, R. W., and T. H. Von der Haar (2001), Interannual variability of cloud forcing and meridional energy transport for the Northern Hemisphere winter from 1984–1990, *J. Clim.*, 14, 3643–3654, doi:10.1175/1520-0442(2001)014<3643:lvocfa>2.0.CO;2.
- Morrison, H., and A. Gettelman (2008), A new two-moment bulk stratiform cloud microphysics scheme in the community atmosphere model, version 3 (CAM3). Part I: Description and numerical tests, *J. Clim.*, 21, 3642–3659, doi:10.1175/2008JCLI2105.1.
- Norris, J. R. (2005), Trends in upper-level cloud cover and surface divergence over the tropical Indo-Pacific Ocean between 1952 and 1997, *J. Geophys. Res.*, 110, D21110, doi:10.1029/2005JD006183.
- Park, S., and C. S. Bretherton (2009), The University of Washington shallow convection and moist turbulence schemes and their impact on climate simulations with the community atmosphere model, *J. Clim.*, 22, 3449–3469, doi:10.1175/2008JCLI2557.1.
- Park, S., and C. B. Leovy (2004), Marine low-cloud anomalies associated with ENSO, *J. Clim.*, 17, 3448–3469, doi:10.1175/1520-0442(2004)017<3448:MLAAWE>2.0.CO;2.
- Park, S., C. S. Bretherton, and P. J. Rasch (2014), Integrating cloud processes in the Community Atmosphere Model, version 5, *J. Clim.*, 27, 6821–6856, doi:10.1175/JCLI-D-14-00087.1.
- Prospero, J. M., and P. J. Lamb (2003), African droughts and dust transport to the Caribbean: Climate change implications, *Science*, 302, 1024–1027, doi:10.1126/science.1089915.
- Ramanathan, V., R. D. Cess, E. F. Harrison, P. Minnis, B. R. Barkstrom, E. Ahmad, and D. Hartmann (1989), Cloud-radiative forcing and climate: Results from the Earth Radiation Budget Experiment, *Science*, 243, 57–63, doi:10.1126/science.243.4887.57.
- Ruckstuhl, C., et al. (2008), Aerosol and cloud effects on solar brightening and the recent rapid warming, *Geophys. Res. Lett.*, 35, L12708, doi:10.1029/2008GL034228.
- Slingo, A. (1990), Sensitivity of the Earth's radiation budget to changes in low clouds, *Nature*, 343, 49–51, doi:10.1038/343049a0.
- Stephens, G. L. (2005), Cloud feedbacks in the climate system: A critical review, *J. Clim.*, 18, 237–273, doi:10.1175/JCLI-3243.1.
- Stephens, G. L., J. Li, M. Wild, C. A. Clayton, N. Loeb, S. Kato, T. L'Ecuyer, P. W. Stackhouse Jr., M. Lebsack, and T. Andrews (2012), An update on Earth's energy balance in light of the latest global observations, *Nat. Geosci.*, 5, 691–696, doi:10.1038/ngeo1580.
- Streets, D. G., F. Yan, M. Chin, T. Diehl, N. Mahowald, M. Schultz, M. Wild, Y. Wu, and C. Yu (2009), Anthropogenic and natural contributions to regional trends in aerosol optical depth, 1980–2006, *J. Geophys. Res.*, 114, D00D18, doi:10.1029/2008JD011624.
- Twomey, S. (1974), Pollution and the planetary albedo, *Atmos. Environ.*, 8, 1251–1256, doi:10.1016/0040-6981(74)90004-3.
- Van der Werf, G. R., J. T. Randerson, L. Giglio, J. G. Collatz, P. Kasibhatla, and A. F. Arellano (2006), Interannual variability in global biomass burning emissions from 1997 to 2004, *Atmos. Chem. Phys.*, 6, 3423–3441, doi:10.5194/acp-6-3423-2006.
- Wielicki, B. A., et al. (1998), Clouds and the Earth's radiant energy system (CERES): Algorithm overview, *IEEE Trans. Geosci. Remote Sens.*, 36, 1127–1141.
- Wu, R., Z. Wen, and Z. He (2013), ENSO contribution to aerosol variations over the maritime continent and the Western North Pacific during 2000–10, *J. Clim.*, 26, 6541–6560, doi:10.1175/JCLI-D-12-00253.1.
- Xie, P., and P. A. Arkin (1997), Global precipitation: A 17-year monthly analysis based on gauge observations, satellite estimates, and numerical model outputs, *Bull. Am. Meteorol. Soc.*, 78, 2539–2558, doi:10.1175/1520-0477(1997)078<2539:GPAYMA>2.0.CO;2.
- Xu, L., D. W. Pierce, L. M. Russell, A. J. Miller, R. C. J. Somerville, C. H. Twomey, S. J. Ghan, B. Singh, J. Yoon, and P. J. Rasch (2015), Interannual to decadal climate variability of sea salt aerosols in the coupled climate model CESM1.0, *J. Geophys. Res. Atmos.*, 120, 1502–1519, doi:10.1002/2014JD022888.
- Yang, Y., H. Liao, and J. Li (2014), Impacts of the East Asian summer monsoon on interannual variations of summertime surface-layer ozone concentrations over China, *Atmos. Chem. Phys.*, 14, 6867–6879, doi:10.5194/acp-14-6867-2014.
- Yang, Y., H. Liao, and S. Lou (2015), Decadal trend and interannual variation of outflow of aerosols from East Asia: Roles of variations in meteorological parameters and emissions, *Atmos. Environ.*, 100, 141–153, doi:10.1016/j.atmosenv.2014.11.004.
- Zelinka, M. D., and D. L. Hartmann (2011), The observed sensitivity of high clouds to mean surface temperature anomalies in the tropics, *J. Geophys. Res.*, 116, D23103, doi:10.1029/2011JD016459.
- Zhang, G. J., and N. A. McFarlane (1995), Sensitivity of climate simulations to the parameterization of cumulus convection in the Canadian Climate Center general circulation model, *Atmos. Ocean*, 33, 407–446.
- Zhu, P., J. J. Hack, J. T. Kiehl, and C. S. Bretherton (2007), Climate sensitivity of tropical and subtropical marine low cloud amount to ENSO and global warming due to doubled CO<sub>2</sub>, *J. Geophys. Res.*, 112, D17108, doi:10.1029/2006JD008174.
- Ziemke, J. R., and S. Chandra (2003), La Niña and El Niño—Induced variabilities of ozone in the tropical lower atmosphere during 1970–2001, *Geophys. Res. Lett.*, 30(3), 1142, doi:10.1029/2002GL016387.